

Department of Aerospace Engineering
The Pennsylvania State University
University Park, PA 16802

LANGLEY GRANT
IN-34-CR
133 330
328

Annual Progress Report on
NASA Grant No. NAG-1-657

Period: 3/1/87-2/29/88

Reynolds Stress Closure in Jet Flows
Using Wave Models

(NASA-CR-182662) REYNOLD STRESS CLOSURE IN
JET FLOWS USING WAVE MODELS Annual Progress
Report, 1 Mar. 1987 - 29 Feb. 1988
(Pennsylvania State Univ.) 32 p CSDL 20D

N88-19741

Unclas
G3/34 0133330

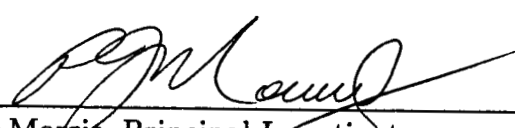
sponsored by

National Aeronautics and Space Administration

Langley Research Center
Hampton, VA 23665

Submitted by:

Date:


P. J. Morris, Principal Investigator
Professor of Aerospace Engineering
233-L Hammond Building
University Park, PA 16802
(814) 863-0157

4/25/88

1. Introduction

During the second year of the research program efforts have continued to concentrate on the development of the numerical methods that will form the computational part of the turbulence closure scheme. Studies have continued on the wave model for the two-dimensional shear layer. This configuration is being used as a test case for the closure schemes. Several numerical schemes for the solution of the non-separable Rayleigh equation have been developed. This solution is required for the closure scheme in more complex geometries. The most efficient method found is a hybrid scheme that combines both pseudospectral and finite difference techniques. In addition, conformal transformation techniques have been developed to transform the arbitrary geometry of the jet to a simple computational domain. We have also continued our study of the shock structure in arbitrary geometry jets and multiple jets. These developments are described briefly below.

2. Numerical Methods for Arbitrary Geometry Jets

In this section we describe the progress we have made in the solution of the non-separable form of the Rayleigh equation. This efficient solution of this equation for arbitrary geometries is a key element in our turbulence closure scheme. The two areas in which progress has been made are (i) the development of a algorithm for the solution of the equation and (ii) the development of conformal transformation methods to transform the jet's arbitrary geometry into a simpler computational domain.

2.1 Numerical Algorithm: Pseudospectral Hybrid Scheme.

A method has been developed to determine the eigensolutions of the Rayleigh equation in flows of arbitrary geometry. The equation to be solved is:

$$(\Delta - \beta^2)p + (2\beta/\Omega)\nabla W \nabla p = 0, \quad (2.1)$$

with boundary conditions:

$$p \text{ is finite and } p \rightarrow 0 \text{ at infinity,} \quad (2.2)$$

where p is the pressure fluctuation, $W(x, y)$ is the axial mean velocity, β is the axial wavenumber, $\Omega = \omega - \beta W$, and ω is the wave frequency. The technique that has been developed to solve (2.1) and (2.2) is a “hybrid” scheme. The method consists of combining a finite difference approximation with a pseudospectral approximation. Consider a solution of the form:

$$p_N = \sum a(x_j, y) f_j(x), \quad (2.3)$$

where the summation is taken over 0 to N . Here the f_j 's are functions defined by:

$$f_j(x) = \frac{(-1)^{j+1}(1-x^2)T'_N(x)}{c_j N^2(x-x_j)}, \quad (2.4)$$

where,

$$x_j = \cos(\pi j/N) \quad \text{for } 0 \leq j \leq N, \quad (2.5)$$

and where T_N is the N -th order Chebyshev polynomial. In addition, $c_0 = c_N = 2$ and $c_j = 1$ for $1 \leq j \leq N-1$.

The discretization of (2.1) is obtained by substituting (2.3) and noticing that (2.4) and (2.5) imply:

$$f_j(x_i) = \begin{cases} 1, & \text{if } j = i; \\ 0, & \text{if } j \neq i. \end{cases} \quad (2.6)$$

The resulting discretization is given by:

$$\begin{aligned} & \{\partial_{yy} + H(x_k, y)\partial_y\}a(x_k, y) - \beta^2 a(x_k, y) \\ & + [\{\partial_{xx} + G(x_k, y)\partial_x\} \sum a(x_j, y) f_j(x)]_{x=x_k} = 0, \end{aligned} \quad (2.7)$$

for $1 \leq k \leq N-1$. In (2.7) the functions H and G are defined in terms of $2\beta/\Omega$ and the components of the gradient of W .

To outline the determination of the eigenvalues β for the Rayleigh problem consider the model shear domain:

$$D := \{(x, y) \in \mathbb{R}^2 \quad -1 \leq x, y \leq 1\}. \quad (2.8)$$

Now, to determine the boundary conditions for the computational domain, D notice that the lines $y \pm 1$ correspond to the edges of the shear layer. On the boundaries of the shear layer the axial mean velocity W becomes constant. Whence, (2.1) reduces to the Helmholtz equation that has a known analytic solution, say:

$$p(x, \pm 1) = \sum R_n(x, \pm 1), \quad (2.9)$$

where R_n would involve Bessel or Hankel functions and exponentials in polar coordinates. In addition, for the lines $x = \pm 1$ a boundary condition based on the periodicity of the pressure fluctuation is assumed. For example of the model domain D , set $p(\pm 1, y) = 0$. This could correspond to pressure fluctuations that are odd about both the major and minor axes of the jet. The determination of the eigenvalues proceeds as follows:

- i) The derivatives in (2.7) for the spectral direction are determined as functions of the collocation points, x_j .
- ii) Equation (2.7) is recast as a two-dimensional vector allowing the use of an explicit integration scheme in the y - direction.
- iii) The function $R_0(x_j, +1)$, from (2.9) and its derivative in the y -direction are evaluated at the collocation points on the line $y = +1$. This gives the initial values for the discretized equations that are then integrated to $y = 0$.
- iv) Step iii) is repeated for the functions $R_n(x_j, +1)$ for $n \leq N - 2$.
- v) Steps iii) and iv) are repeated, starting the integration at $y = -1$ and using the functions $R_n(x_j, -1)$ as the starting conditions.
- vi) The integrated solutions are then matched at $y = 0$. The matching of the solutions and their derivatives gives a $2N \times 2N$ matrix, $\mathbf{M}(\beta)$.

vii) The value of β satisfying $\det[\mathbf{M}(\beta)] = 0$ for a fixed frequency is then computed by providing a first guess for β and then iteratively repeating steps iii) through vi) updating the value β after each iteration.

A code implementing this “hybrid” scheme has been developed for circular and elliptic geometries. The code has been validated for the circular case and in some elliptic cases. Further verification of the elliptic jet case is depends on the coordinate transformations described below. For the circular jet a velocity profile of the form:

$$W(r) = (1 + \tanh[(1 - r)/2\theta])/2, \quad (2.10)$$

has been assumed, where θ is the momentum thickness of the mixing layer. The elliptic test case assumes an ellipse of aspect ratio 2 at the half velocity point of the mean velocity profile.

2.2 Computational Domains for Jets of Arbitrary Geometry

2.2.1. Introduction – An efficient method establishing the computational domain for jets of arbitrary geometry is currently being developed. The technique to be used involves generating conformal mappings which carry standard computational domains into the cross sections of a given jet.

To begin the discussion, the general types of geometries encountered in jet flows will be outlined. Two topologically distinct cross sections occur in a jet. The first type of cross section corresponds to the annular shear region surrounding the jet’s potential core. Since the velocity in the potential core is approximately uniform, the computation needs only to be performed in the annular shear region. Therefore, annular domains constitute the first type of geometry in jet flows: doubly connected regions.

The second general type of geometry encountered in jet flows corresponds to the region of a jet downstream of the potential core. In this case, the computation must be performed

in the entire cross section of the flow. Thus, the second class of geometry are the simply connected, disc-like regions.

The goal of the research on jet geometry is to establish coordinate transformations which map standard computational regions into cross sections of a arbitrary jet. The standard regions are chosen to support the numerical solution of the equations modeling jet flows. Since an arbitrary jet has two distinct types of geometries, two standard types of conformal maps and computational regions result. The following sections will outline the two types of conformal maps to be used and give an example for the doubly connected region of an elliptic jet.

2.2.2. Simply Connected Regions – The standard computational region for this case is the unit disc centered at the origin of the complex plane. A conformal transform, F , mapping the unit disc into a simply connected jet cross section will be generated numerically using a generalization of the method of Theodorsen ref. 1. To understand the geometry, consider Figure 1. Theodorsen's map carries the circle in the computational domain onto the outer edge of the shear layer in physical space.

Let the boundary of the jet cross section be described in polar coordinates in physical space as:

$$w = w(\phi) = R(\phi) \exp(i\phi), \quad (2.11)$$

where, $R(\phi)$ is assumed to be a 2π periodic function, and the region bounded by $R(\phi)$ is required to be *starlike* with respect to the origin. From the development of Henrici ref. 2, Theodorsen's method goes as follows:

i) Assume the conformal map takes the form of:

$$F(z) = z \exp[h(z)], \quad (2.12)$$

where $H(z)$ is an unknown function to be approximated.

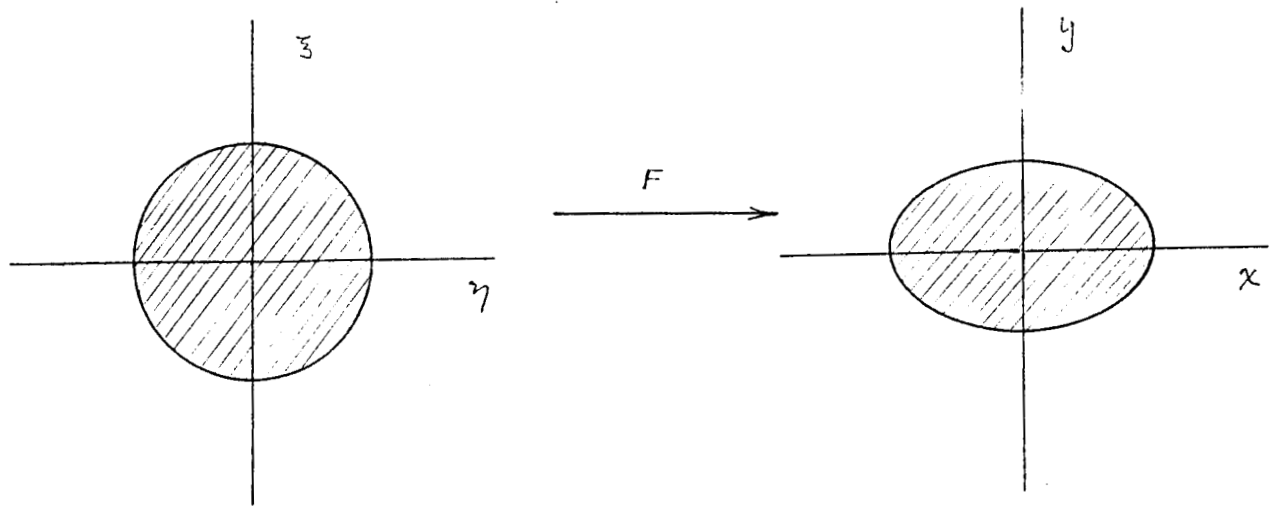


Figure 1: Sketch of Transformation for Simply Connected Domain

ii) Evaluate (2.12) on the unit circle to obtain:

$$\begin{aligned}\Re H[\exp(i\theta)] &= \ln\{R[\phi(\theta)]\}, \\ \Im H[\exp(i\theta)] &= \phi(\theta) - \theta.\end{aligned}\tag{2.13}$$

iii) Next, solve for the relation between the angle ϕ , in physical space and the angle, θ , in computational space which may be shown to be expressed as:

$$\phi(\theta) - \theta = \mathbf{K} \ln\{R[\phi(\theta)]\},\tag{2.14}$$

where \mathbf{K} denotes the principal value integral:

$$\mathbf{K}\phi(x) = \frac{1}{2\pi} \int_0^{2\pi} \phi(y) \cot[(x-y)/2] dy.\tag{2.15}$$

iv) Once equation (2.14) is known, equation (2.12) is used to generate the mapping from the disc to the jet cross section.

Equation (2.14) is solved numerically by introducing the iterative equation:

$$\Delta_{k+1}(\phi) = \mathbf{K} \ln\{R[\theta + \Delta_k(\theta)]\},\tag{2.16}$$

for $k = 0, 1, 2, \dots$, where $\Delta(\theta) \stackrel{\text{def}}{=} \phi(\theta) - \theta$. At each step an FFT is used to approximate (2.16). An initial guess for Δ_k is given by

$$\Delta_0(\theta) = \theta.$$

2.2.3. Doubly Connected Regions – The standard doubly connected computational domain is the circular annulus. The annulus will be normalized such that the outer boundary has radius one. The inner boundary radius, denoted by μ , cannot be chosen arbitrarily but must be determined by the method used to construct the conformal map from the annulus to the jet cross section. The method developed by Theodorsen for simply connected domains was extended by Garrick ref. 3 to generate conformal transformations for annular

regions. The Theodorsen - Garrick scheme is the method that will be employed for doubly connected jet cross sections. The geometry is shown in Figure 2

The Theodorsen - Garrick map, Γ , carries the outer boundary of the annulus onto the outer boundary of the jet cross section. Likewise, the inner annular boundary is assigned to the jet's inner cross section boundary.

To develop the map Γ , let

$$z_i = R_i(\phi) \exp(i\phi) \quad \text{for } i = 0, 1, \quad (2.17)$$

denote 2π periodic functions describing the boundaries of the jet cross section. It is required that the region, bounded by these functions, be *starlike*. Referring to Henrici ref. 2, the construction of Γ goes as follows:

- i) Assume that there exists a conformal map of the form:

$$\Gamma(z) = z \exp[G(z)], \quad (2.18)$$

where $G(z)$ is the unknown function to be approximated.

- ii) Since G is defined on an annulus, it will have a Laurent series of the form:

$$G(z) = a_{0,0} + 2 \sum_{\substack{\text{inf ty} \\ x \neq 0}}^{\infty} A_n z^n, \quad (2.19)$$

where

$$A_n = (a_{0,n} - \mu^n a_{1,n}) / (1 - \mu^{2n}). \quad (2.20)$$

The $a_{i,n}$'s, $i = 0, 1$, depend on the Fourier coefficients of the logarithm of the boundary functions given by (2.17). However, these Fourier coefficients depend on the angle, θ , in the computational domain, and may not be directly computed until a relation of the form $\phi(\theta) = f(\theta)$ is known.

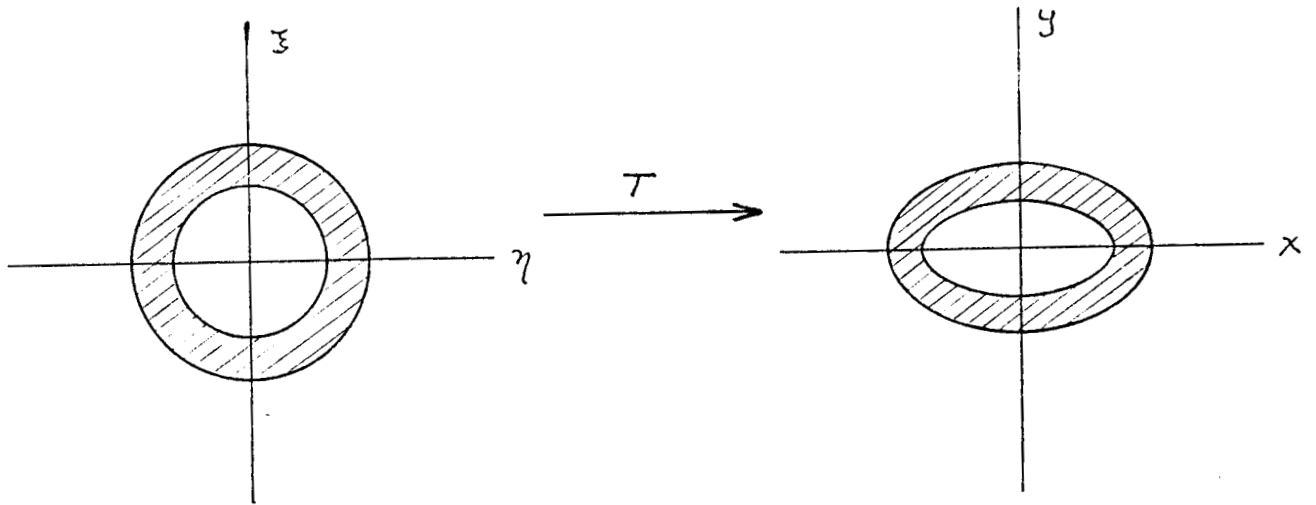


Figure 2: Sketch of Transformation for Doubly Connected Domain

iii) Therefore, a relationship between ϕ and θ must be determined. This is given by the pair of integral equations:

$$\begin{aligned}\phi_0(\theta) - \theta &= \mathbf{H}_\mu \ln\{R_0[\phi_0(\theta)]\} - \mathbf{G}_\mu \ln\{R_1[\phi_1(\theta)]\}, \\ \phi_1(\theta) - \theta &= \mathbf{G}_\mu \ln\{R_0[\phi_0(\theta)]\} - \mathbf{H}_\mu \ln\{R_1[\phi_1(\theta)]\}.\end{aligned}\tag{2.21}$$

Here,

$$\begin{aligned}\mathbf{H}_\mu &= \mathbf{K}\phi(\theta) + \mathbf{K}_\mu\phi(\theta), \\ \mathbf{G}_\mu\phi(\theta) &= \mathbf{K}_\mu\phi(\theta),\end{aligned}\tag{2.22}$$

where \mathbf{K} is defined as in equation (2.15) and

$$\mathbf{K}_\mu\phi(\theta) = \frac{1}{\pi} \int_{-\pi}^{\pi} \phi(\beta) k_\mu(\theta - \beta) d\beta,$$

and where,

$$k_\mu(x) = \sum_{n=1}^{\infty} (2\mu^{2n} / (1 - \mu^{2n}) \sin(nx)).$$

Finally, μ is given by:

$$\mu = \exp \left\{ \frac{1}{2\pi} \int_0^{2\pi} \ln\{R_1[\phi_1(\theta)]\} / R_0[\phi_0(\theta)] d\theta \right\}.\tag{2.23}$$

iv) Once equations (2.21) to (2.23) have been solved for ϕ_i and for μ the Fourier coefficients for $\ln\{R_i[\phi_i(\theta)]\}$ can be determined and substituted into equation (2.19) to give the Laurent series for $G(z)$. Combining G with equation (2.18) then gives the desired conformal map.

This set of nonlinear integral equations can be rapidly solved for the angle variations, ϕ_i , and for μ by using the iterative approximation to equations (2.21):

$$\begin{aligned}\phi_{0,m+1} - \theta &= \mathbf{H}_\mu \ln[R_0(\phi_{0,m})] - \mathbf{G}_\mu \ln[R_1(\phi_{1,m})], \\ \phi_{1,m+1} - \theta &= \mathbf{G}_\mu \ln[R_0(\phi_{0,m})] - \mathbf{H}_\mu \ln[R_1(\phi_{1,m})],\end{aligned}\tag{2.24}$$

where for an approximated μ the operators defined by equations (2.22) are determined. The iterative scheme is very efficient because, all of the functions considered are approximated

using an FFT. At each step in the iteration a new value of μ is given by the exponential of the difference of the zero coefficients in the Fourier series, of the functions, $\ln\{R_i[\phi_{i,m}(\theta)]\}$.

2.2.4. General Remarks – The iterative schemes described in the sections above converge very rapidly for nearly circular regions. However, as the physical domains become more eccentric, i.e., for high aspect ratios, the methods converge slowly, and in some cases, not at all. This problem is fairly easy to overcome by using preliminary conformal transformations which carry the physical domain into a region which has a lower aspect ratio. Moreover, all the iteration schemes may be recast using underrelaxation. Details of the underrelaxation technique for simply connected regions are described in Gutknecht ref. 4.

It should be recalled that conformal maps locally preserve the angles between mapped curves. Therefore, an orthogonal coordinate grid in the computational domain will translate into an orthogonal grid in the physical space. Since the coordinates are orthogonal, the metric tensor associated with conformal maps will have only diagonal terms which are nontrivial. Therefore, conformal maps introduce a minimum number of derivative terms in the transformed equations of motion.

2.2.5. Example – In this section an example of the conformal transform mapping the annulus onto a shear layer bounded by two confocal ellipses will be examined. The ellipses are defined by:

$$x^2 + (4/3)y^2 = 1, \quad (2.25)$$

$$(16/9)x^2 + (16/5)y^2 = 1. \quad (2.26)$$

Equation (2.25) defines the outer edge of the shear layer, while equation (2.26) defines the inner edge. In order to estimate the accuracy of the map, an error measure will be defined for the points mapped to the boundaries of the cross section. Therefore, set

$$\text{Error Measure} \stackrel{\text{def}}{=} |F[\Gamma(R, \theta)] - 1|,$$

where F denotes either equation (2.25) or (2.26) and $R = 1$ or μ depending on F . Let N denote the number of data points used to compute the FFT of the boundary functions, and let θ denote the angle in the computational space. Calculations of the error measure are given in Table 1.

The following figures, 3a and 3b, show a computational grid and its image in the physical domain for the numerical example exhibited here. For the figures: $N=1024$ and the error is $\approx O(10^{-5})$.

2.3 Shock Structure in Arbitrary Geometry Jets

Models have also been developed to describe the shock structure and instability waves in single and multiple jets of arbitrary geometry. The initial results of this study were given by Morris, Bhat and Chen ref. 5. This paper, which is attached as an appendix to this report, described the use of a boundary element method to determine the shock spacing in jets of arbitrary geometry represented by a vortex sheet. This topic has been submitted for publication in the **Journal of Sound and Vibration**. At present we are extending the analysis to include the effects of finite mixing region thickness and the effects of the small-scale turbulence for both single and multiple jets. The results for the finite mixing layer thickness are described here.

2.3.1 Effects of finite mixing layer thickness on shock structure in jets of arbitrary geometry – A finite difference technique has been developed to study the shock structure and hydrodynamic stability of jets with arbitrary exit geometry. A body-fitted coordinate system is used which is particularly suited for problems associated with arbitrary exit geometry. This finite difference scheme includes the effect of a finite mixing layer thickness by using a realistic and continuous mean

Case 1: The image of the circle of $R = \mu$

N	θ	x	y	Error
64	0	.749165	.000000	.002230
128	0	.749791	.000000	.000590
256	0	.749947	.000000	.000139
512	0	.749986	.000000	.000035
64	$\pi/4$.528549	.394927	.004254
128	$\pi/4$.529897	.395195	.001042
256	$\pi/4$.530222	.395262	.000260
512	$\pi/4$.530112	.395278	.000067
64	$\pi/2$.000000	.562340	.011924
128	$\pi/2$.000000	.559885	.003110
256	$\pi/2$.000000	.559236	.000787
512	$\pi/2$.000000	.559072	.000197

Case 2: The image of the circle $R = 1$

N	θ	x	y	Error
64	0	.999086	.000000	.001826
128	0	.999771	.000000	.000457
256	0	.999943	.000000	.000114
512	0	.999985	.000000	.000028
64	$\pi/4$.706094	.612594	.001068
128	$\pi/4$.706856	.612424	.000270
256	$\pi/4$.707044	.612385	.000068
512	$\pi/4$.707091	.612375	.000017
64	$\pi/2$.000000	.867770	.004034
128	$\pi/2$.000000	.866468	.001023
256	$\pi/2$.000000	.866136	.000256
512	$\pi/2$.000000	.866053	.000064

Case 3: The value of μ

N	μ
64	.701323
128	.701456
256	.701489
512	.702497

COMPUTATIONAL DOMAIN

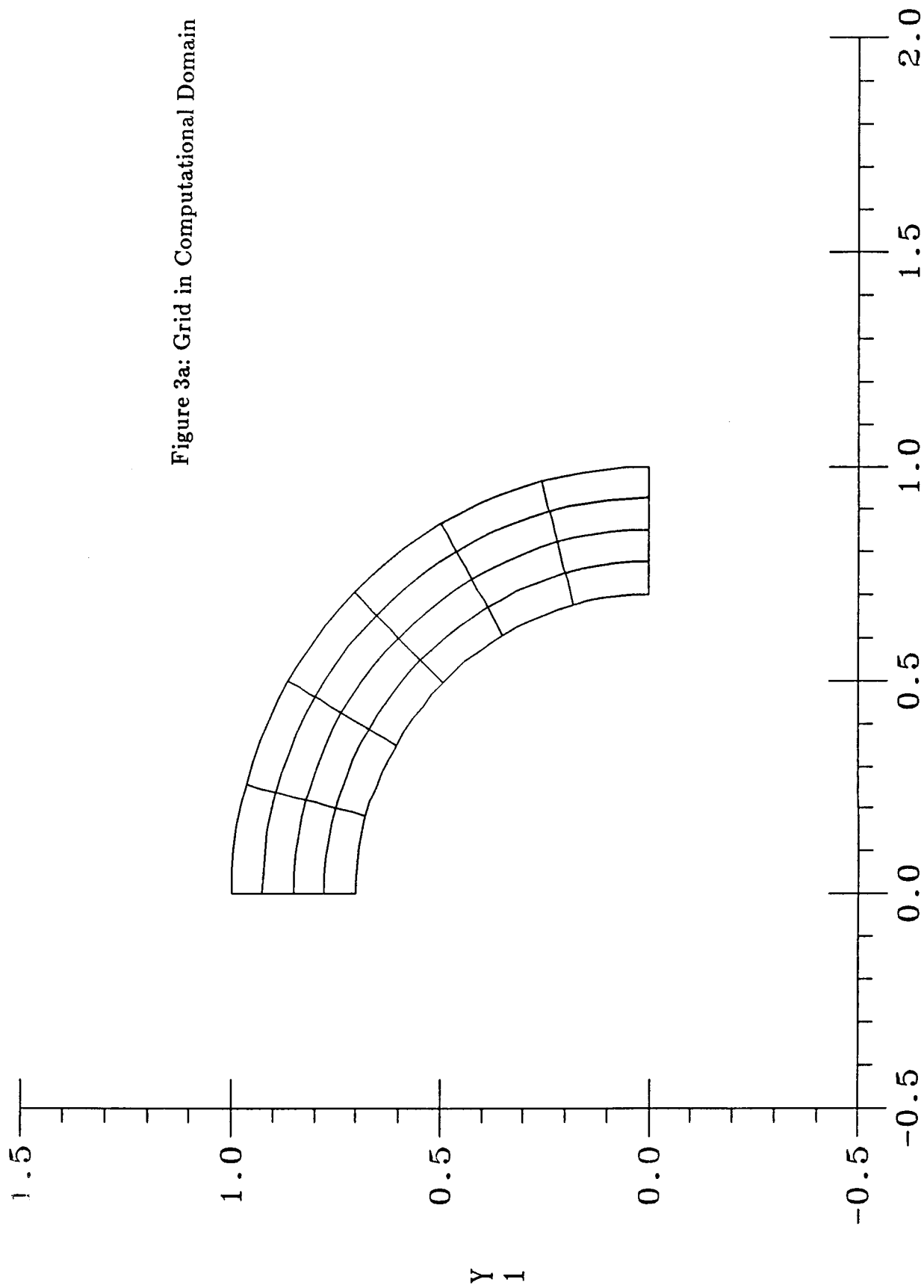


Figure 3a: Grid in Computational Domain

PHYSICAL DOMAIN

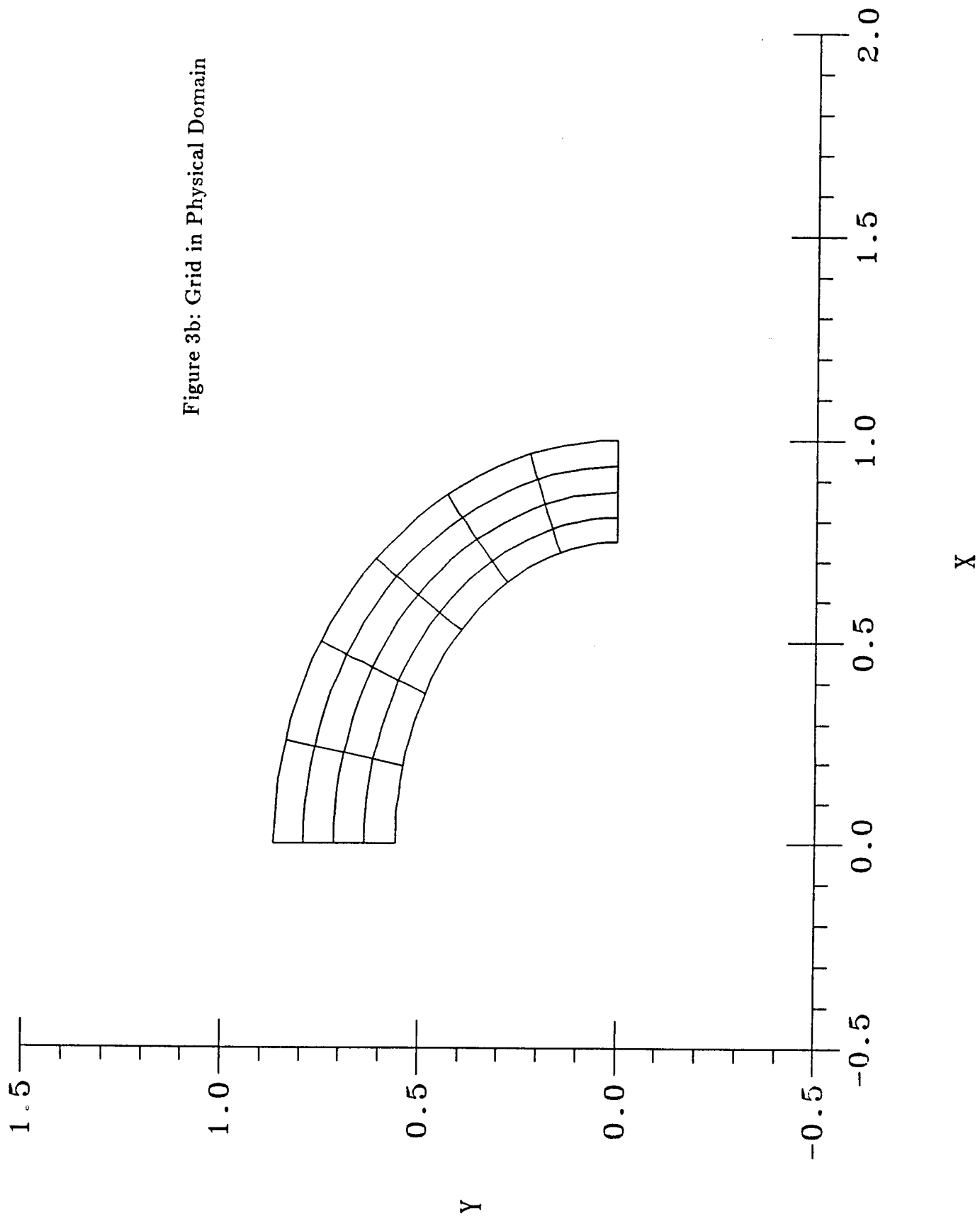


Figure 3b: Grid in Physical Domain

profile. The method and the results for circular and elliptic jets are described below.

Figure 4 shows the regions of a typical jet cross-section and the curvilinear coordinate system. The potential core region is bounded by the curve C_1 and an (s, n) coordinate system is used to represent it. The mixing layer is bounded by the curve C_2 . The coordinates s and n are measured along and normal to the curve C_1 respectively. The radius of curvature, R of curve C_1 is a function of s only. Thus, the equation describing the curve C_1 is all that is required to describe the coordinate system.

The governing equations for a compressible, inviscid fluid including the curvature effects are given by,

$$\begin{aligned} \frac{\partial \rho}{\partial t} + (1 + n/R)^{-1} \frac{\partial}{\partial s}(\rho u) + \frac{\partial}{\partial n}(\rho v) + \frac{\rho v}{(1 + n/R)} + \frac{\partial}{\partial z}(\rho w) &= 0. \\ \rho \frac{\partial u}{\partial t} + \frac{\rho u}{(1 + n/R)} \frac{\partial u}{\partial s} + \rho v \frac{\partial u}{\partial n} + \rho w \frac{\partial u}{\partial z} + \frac{\rho u v}{(1 + n/R) R} &= - \frac{1}{(1 + n/R)} \frac{\partial p}{\partial s}. \\ \rho \frac{\partial v}{\partial t} + \frac{\rho u}{(1 + n/R)} \frac{\partial v}{\partial s} + \rho v \frac{\partial v}{\partial n} + \rho w \frac{\partial v}{\partial z} - \frac{\rho u^2}{(1 + n/R) R} &= - \frac{\partial p}{\partial n}. \\ \rho \frac{\partial w}{\partial t} + \frac{\rho u}{(1 + n/R)} \frac{\partial w}{\partial s} + \rho v \frac{\partial w}{\partial n} + \rho w \frac{\partial w}{\partial z} &= - \frac{\partial p}{\partial z}. \\ \rho C_p \left[\frac{\partial T}{\partial t} + \frac{u}{(1 + n/R)} \frac{\partial T}{\partial s} + v \frac{\partial T}{\partial n} + w \frac{\partial T}{\partial z} \right] &= \\ \left[\frac{\partial p}{\partial t} + \frac{u}{(1 + n/R)} \frac{\partial p}{\partial s} + v \frac{\partial p}{\partial n} + w \frac{\partial p}{\partial z} \right]. \end{aligned}$$

Where (u, v, w) are the velocity components in the (s, n, z) directions respectively, and p and T are the thermodynamic pressure and temperature respectively.

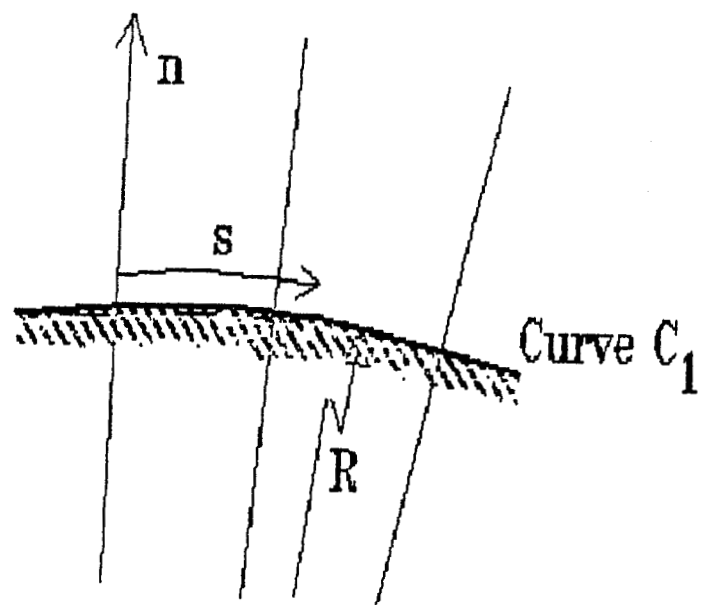
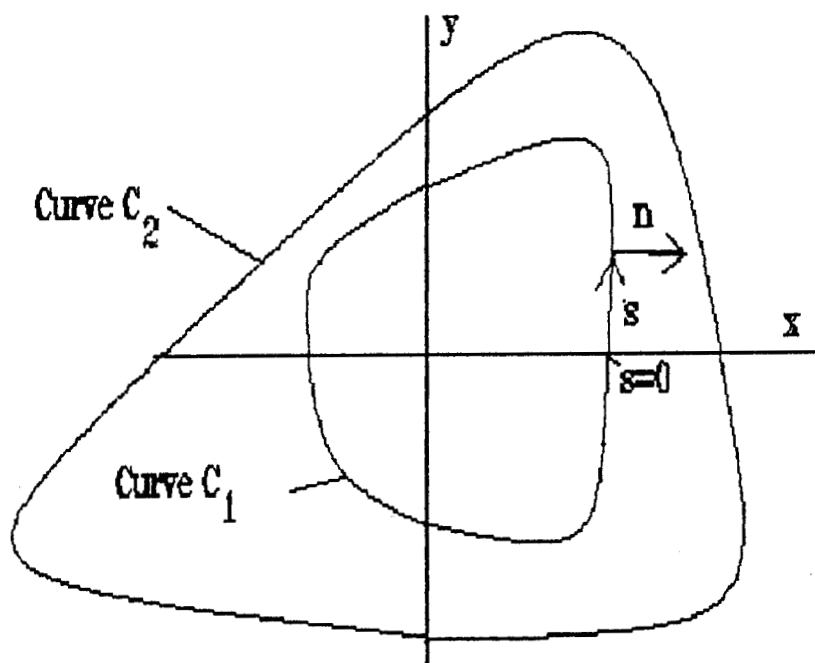


Figure 4: Sketch of Jet Cross Section and Coordinate System.

The general form of separable solution for the fluctuating pressure, when the mean velocity and density are taken to be independent, locally, of the axial distance is given by:

$$p(s, n, z, t) = \hat{p}(s, n) \exp[i(kz - \omega t)],$$

where k is a wavenumber and ω is the radian frequency.

The pressure fluctuation then satisfies the Rayleigh equation,

$$\frac{\partial^2 \hat{p}}{\partial n^2} + \frac{1}{(1 + n/R)} \frac{\partial \hat{p}}{\partial n} + \frac{1}{(1 + n/R)^2} \frac{\partial^2 \hat{p}}{\partial s^2} + \frac{2k}{\Omega} \left\{ \frac{1}{(1 + n/R)^2} \frac{\partial U}{\partial s} \frac{\partial \hat{p}}{\partial s} + \frac{\partial U}{\partial n} \frac{\partial \hat{p}}{\partial n} \right\} - (k^2 - \bar{\rho} M_j^2 \Omega^2) \hat{p} = 0,$$

where, $\Omega = (\omega - kU)$ and the flow is assumed to be isothermal. This latter restriction may be readily removed.

For an arbitrarily shaped jet U is a function of both s and n . Thus a separable solution in s and n is generally not available and one resorts to a numerical solution in the mixing layer. Along the interior edge of this region and in the potential core of the jet, the mean velocity is a constant. In the ambient fluid surrounding the jet the properties are also uniform. Thus on the inner and the outer boundaries of the mixing layer, a separable form of solution may be obtained. In general, a separable form of solution cannot be obtained in the (s, n) coordinate system. Thus, the general separable solution is obtained in (r, θ) polar coordinates and the relationship between the (r, θ) and (s, n) coordinates is used to transform the solution to the (s, n) coordinate system. This doesn't pose any extra problems while dealing with arbitrary exit geometries.

2.3.2 Numerical Calculations – The numerical method used here is identical to that used earlier, ref. 5, and hence, the details of the method are not given here. The

only difference is that we are now integrating along lines normal to the potential core and not along radial lines.

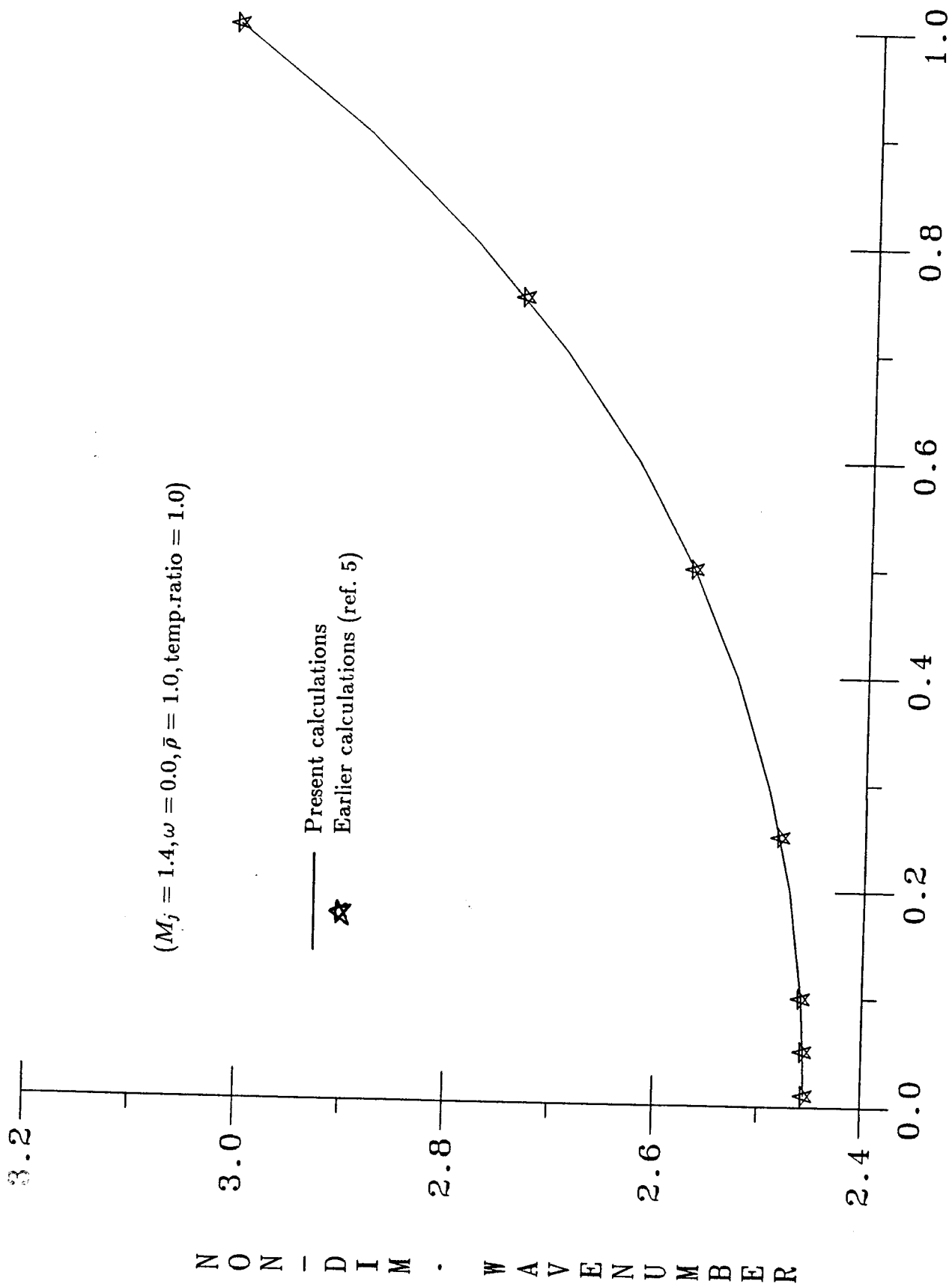
The mean velocity profile is taken to be,

$$U(n) = U_j \exp[-\ln 2(\eta)^2], \quad \text{where} \quad \eta = n/b.$$

b is the local half-width of the jet mixing layer. The relationship between h , the potential core radius, and b is obtained from an integral form of the axial momentum equation.

Figures 5, 6 and 7 show the variation of the axial wave number (lowest), which is inversely related to the shock spacing, as a function of mixing layer thickness and Mach number. Figure 5 shows the result for a circular jet at $M_j = 1.4$ and it can be seen that it compares well with the earlier work. Figure 6 compares the results for an elliptic jet of aspect ratio = 2. For small values of b the spacing approaches that given by the vortex sheet model. Here, comparison is made with the results from the vortex sheet model and for $b = 0.01$ and 0.001 . The agreement is very good for the Mach number range considered. Figure 7 shows the results for a circular jet and an elliptic jet of aspect ratio = 2. In all these cases, only the lowest wave number associated with the axisymmetric mode has been sought.

The results obtained here using the (s, n) coordinate system are in good agreement with the earlier work. The advantage of this method is that it is particularly suited for problems posed by arbitrary exit geometry. It should be noted that an inviscid model is used here and thus the calculations do not reflect the dissipative effect of the shear layer turbulence. The next stage of analysis is to include this viscous effect which would simply convert the equation satisfied by the pressure fluctuations from the Rayleigh equation to an Orr-Sommerfield equation.



MIXING LAYER THICKNESS B/RJ

Figure 5: Variation of Shock Spacing in Circular Jet with Mixing Layer Width.

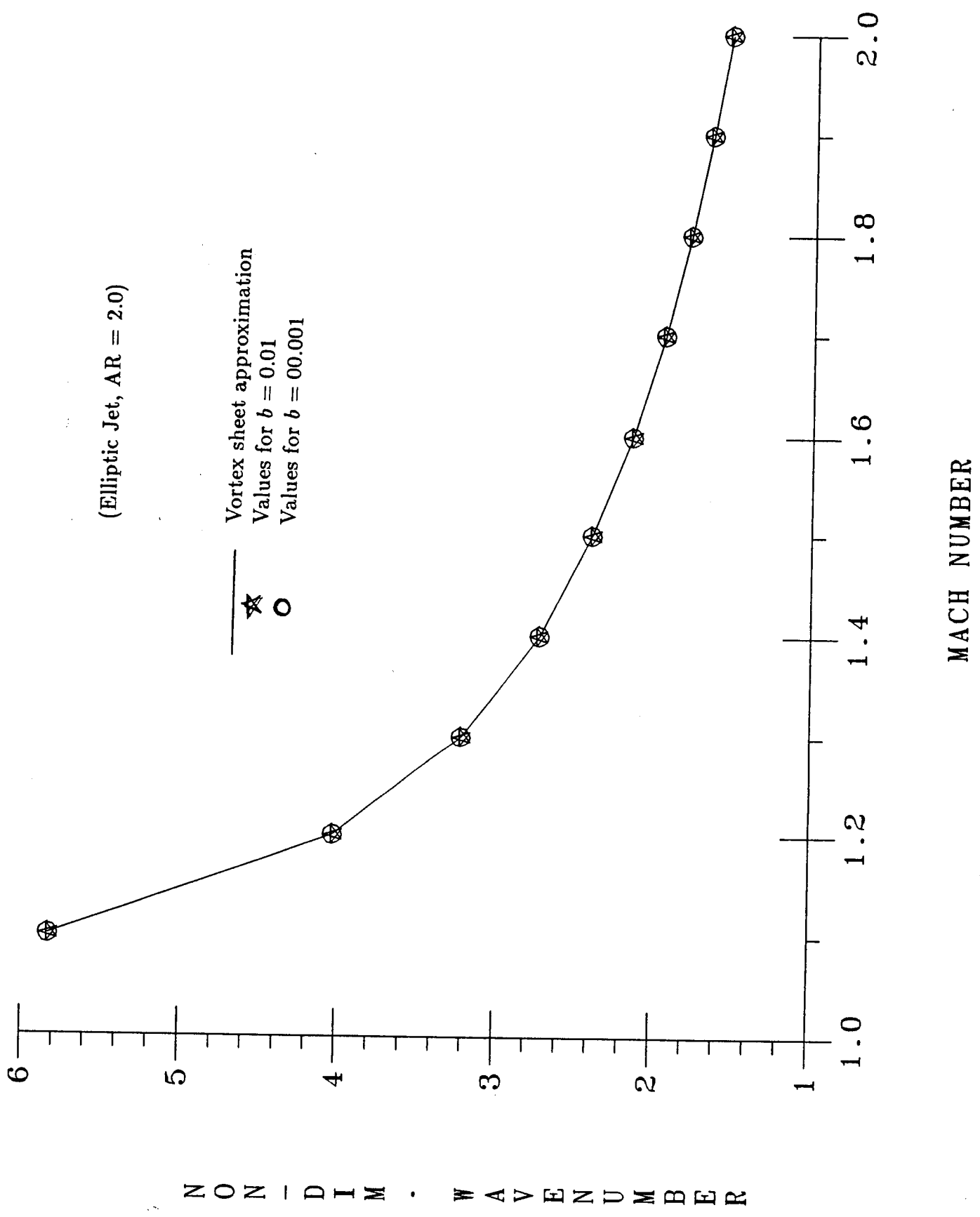
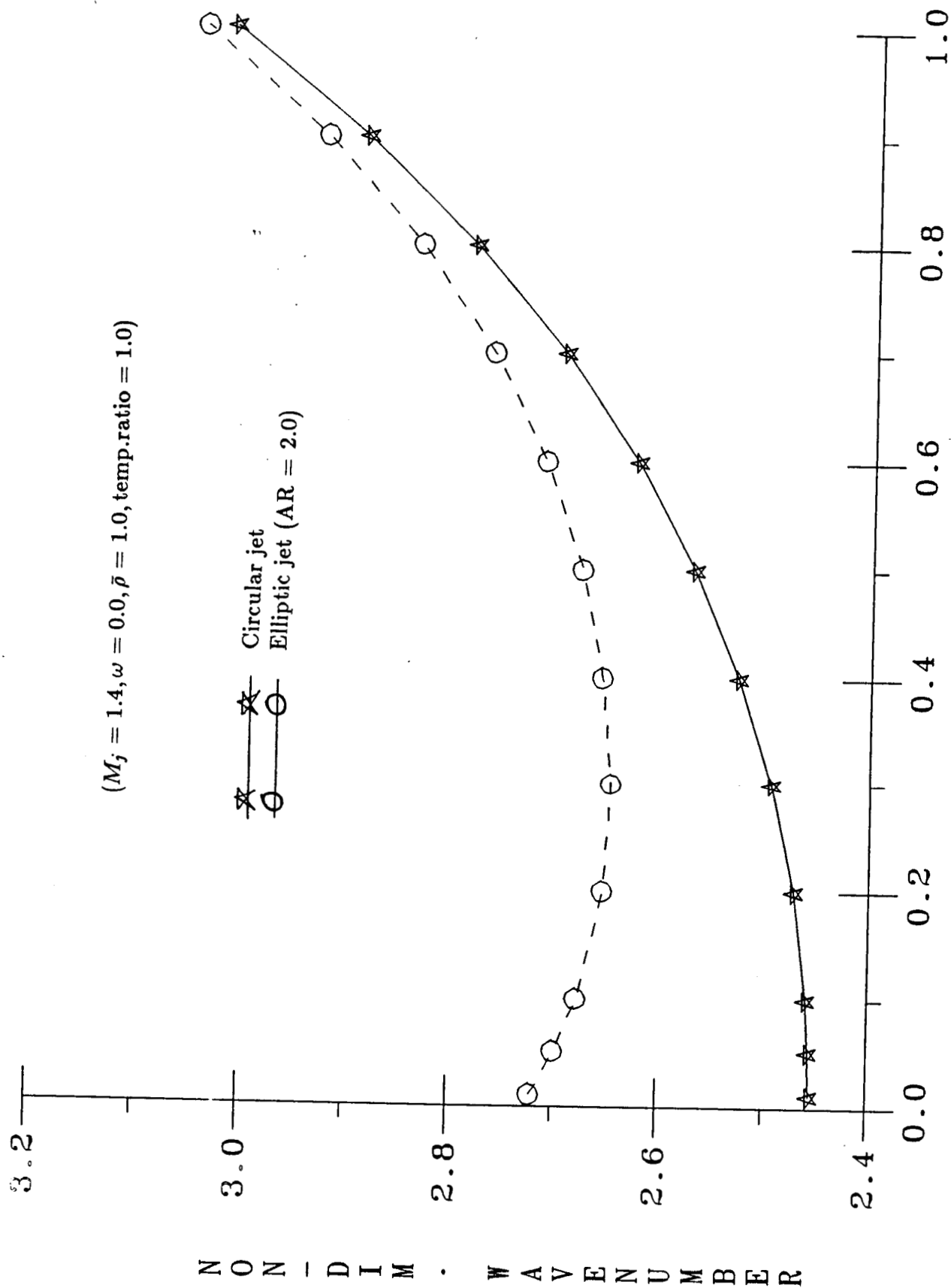


Figure 6: Variation of Shock Spacing in Elliptic Jet with Mach Number.

CIRCULAR & ELLIPTIC JET



MIXING LAYER THICKNESS B/RJ
 Figure 7: Variation of Shock Spacing in Elliptic and Circular Jets with Mixing Layer Thickness.

The method described here can be used for other jet geometries, but at present, due to lack of experimental mean flow data at high speeds, it has not been implemented for, say rectangular and triangular jets.

3. Turbulence Closure Scheme

This part of the work is concerned with the prediction of the mean flow properties of turbulent circular jets. A wave model is used to simulate the large-scale, coherent structures that dominate not only jets but also other free shear flows like mixing layers and wakes. Once the modeling procedure has been developed it will be extended to more complex geometries using the methods described in the preceding sections. At the present stage we are focussing on the validation of the wave model and the development of an in-depth understanding of the physical characteristics of the wave structures. This is being assisted by studying a two-dimensional incompressible free mixing layer. This will provide guidelines for more complex applications of the model. The equations used in the present wave model formulation are the continuity and the momentum equations of the long time-averaged properties for the mean flow, U_i , and of the wave-like large-scale structures, u_i . These are

$$\frac{\partial U_i}{\partial x_i} = \frac{\partial u_i}{\partial x_i} = 0 ,$$

$$U_j \frac{\partial U_i}{\partial x_j} + \frac{\partial}{\partial x_j} \overline{u_i u_j} + \frac{\partial}{\partial x_j} \overline{u_i' u_j'} = -\frac{1}{\rho} \frac{\partial P}{\partial x_i} + \nu \frac{\partial^2 U_i}{\partial x_j \partial x_j} .$$

where

$$\bar{q} = Q = \frac{1}{T_1} \int_0^{T_1} q dt, \quad T_1 \rightarrow \infty.$$

The nonlinear wave development may be simulated by introducing an amplitude function $A(x)$ and describing the large-scale coherent structures in wave-like form:

$$\{u, v\} = A(x) \Re\{[\phi(y), \psi(y)] \exp[i(\alpha x - \omega t)]\}.$$

The amplitude of the wave-like disturbances is determined by the kinetic energy equation for the large-scale motions,

$$\begin{aligned} U_j \frac{\partial k}{\partial x_j} = & -\overline{u_i u_j} \frac{\partial U_i}{\partial x_j} - \frac{\partial}{\partial x_j} (\overline{u_j k} + \frac{\overline{p u_j}}{\rho}) - \overline{(- < -u'_i u'_j >) \frac{\partial u_i}{\partial x_j}} \\ & - \frac{\partial}{\partial x_j} (\overline{u_i < u'_i u'_j >}) + \text{viscous terms} \end{aligned}$$

where

$$< q > = \frac{1}{T_2} \int_0^{T_2} q \, dt, \quad T_2 \ll T_1$$

Our previous calculations, ref. 6 have shown that the influence of the small-scale structures cannot be neglected. This is especially important on the low-velocity side of the mixing layer. It has also been shown experimentally ref. 7 that the contribution to the long time-averaged Reynolds stresses from the large and small scale components may be equally important in fully-developed mixing layers. A *split-spectrum* approach was thus adopted ref. 8, which assumes that some of the turbulent kinetic energy is contained in the small-scale motions. A computer program implementing an interactive approach that links the long time-averaged flow, the wave-like, large-scale motions, and the small-scale fluctuations has been developed. The small-scale, non-coherent stresses may be modeled initially using an eddy-viscosity formulation, that is,

$$\overline{u'_i u'_j} = 2 \nu \overline{S_{ij}}$$

The starting mean velocity profile was taken from experimental results for a free mixing layer. It was found that in the long tail region of the velocity profile the negative production of the large-scale structures prevented the flow from accelerating and stopped the mixing region from growing. Figure 8 gives the mean velocity profiles in the streamwise direction. The deceleration effect can be clearly seen. Similar results were found for a two-stream mixing layer. For a free mixing layer, the accuracy of the measured mean flow data on the low-speed are subject to error due to the rapid variations in the instantaneous flow direction. Thus it is possible that the waves driven by the mean flow see a “mean” different from that obtained from a long time-average, especially at places where the fluctuations may actually modify the “mean” flow as they pass by.

We also found that the amplitude of the waves grew exponentially. It is known from experiments, however, that the amplitude grows exponentially for only a short distance downstream before saturating. In our models it is the residual stress tensor γ_{ij} which appears in the wave kinetic energy equation in the form

$$-\gamma_{ij} \frac{\partial u_i}{\partial x_j}$$

that is responsible for the draining of the energy from the waves. The residual stresses were simulated by the eddy-viscosity model. The constant in the model was taken to be the same as that in the eddy-viscosity model for the small-scale Reynolds stresses. It was found that the term thus calculated was far too small to represent the amount of energy that would be transferred from the large-scale to

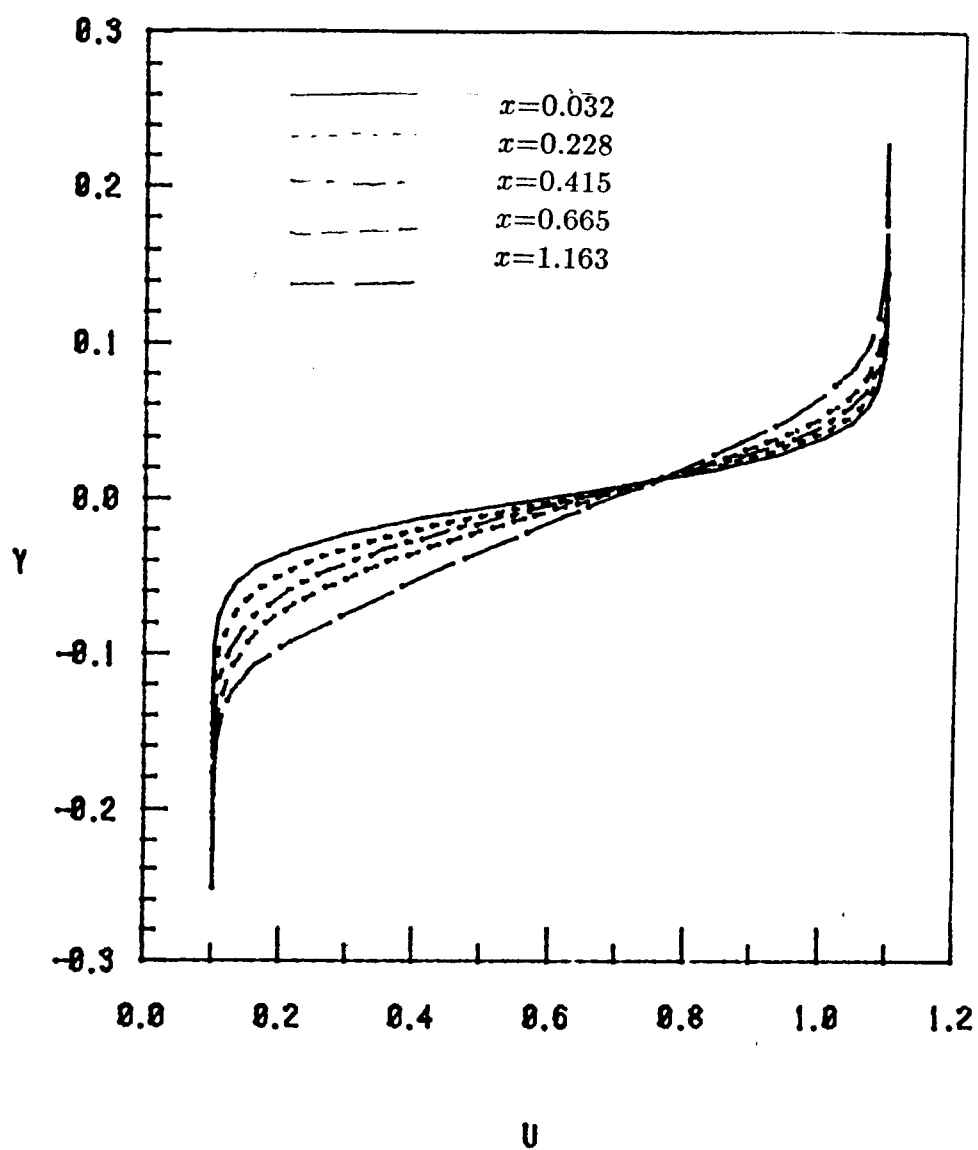


Figure 8: Variation of Mean Velocity with Axial Distance.

that is responsible for the draining of the energy from the waves. The residual stresses were simulated by the eddy-viscosity model. The constant in the model was taken to be the same as that in the eddy-viscosity model for the small-scale Reynolds stresses. It was found that the term thus calculated was far too small to represent the amount of energy that would be transferred from the large-scale to the small-scale motions. The amplitude of the waves, therefore, grew essentially without limit. To verify this, we simulated the gross effects of this term by

$$- C \frac{k^{3/2}}{l}$$

where C is a constant and l is a local length scale. This is based on dimensional reasoning and the assumption that the γ_{ij} scale with the kinetic energy, k , of the wave motions. Part of the turbulent kinetic energy is then taken away from the motion of the wavy components and limits their amplitude. Figure 9 shows the development of the mean stream-wise velocity component calculated using this model. We also compared the variations of the wave amplitude in these two cases. The results are shown in figure 10. The amplitude function initially grows exponentially and then flattened. This agrees with experimental findings, ref. 8. Thus, a good model for these residual stresses is crucial since the coherent structures dominate the flow development and their amplitude must be determined. Unfortunately, little experimental data is available regarding these stresses.

Several approaches are now being developed to model this energy transfer mechanism. On-going efforts also include using the kinetic energy equation for the small-scale motion to estimate the velocity scale in the eddy viscosity model. The equation for the small-scale turbulent kinetic energy is

$$U_j \frac{\partial k'}{\partial x_j} = -\overline{u'_i u'_j} \frac{\partial u_i}{\partial x_j} - \frac{\partial}{\partial x_j} (\overline{u'_j k'} + \frac{\overline{p' u'_j}}{\rho}) + \overline{(- < -u'_i u'_j >) \frac{\partial u_i}{\partial x_j}} \\ - \overline{u_j \frac{\partial}{\partial x_j} < \frac{1}{2} u'_i u'_i >} + \text{viscous terms}$$

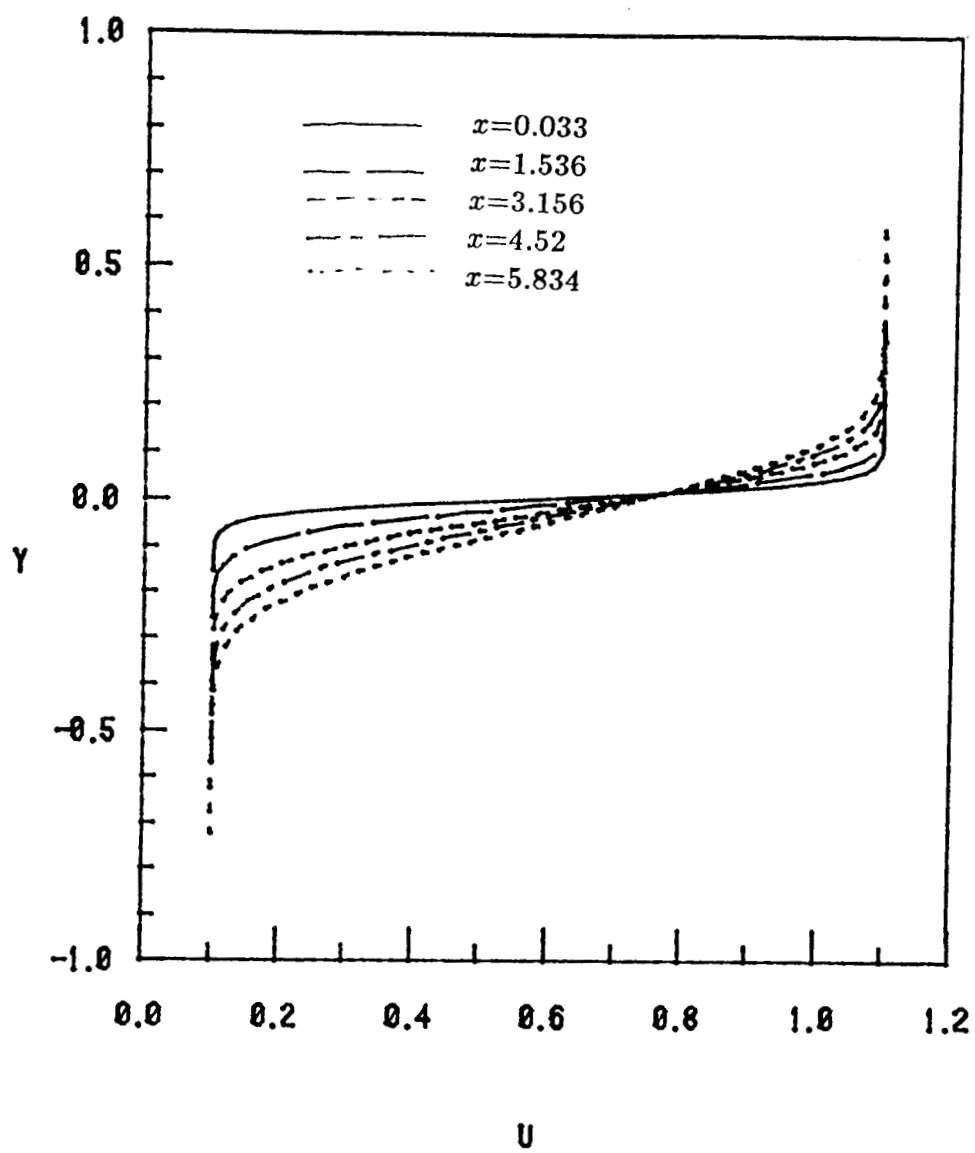


Figure 9: Variation of Mean Velocity with Axial Distance.

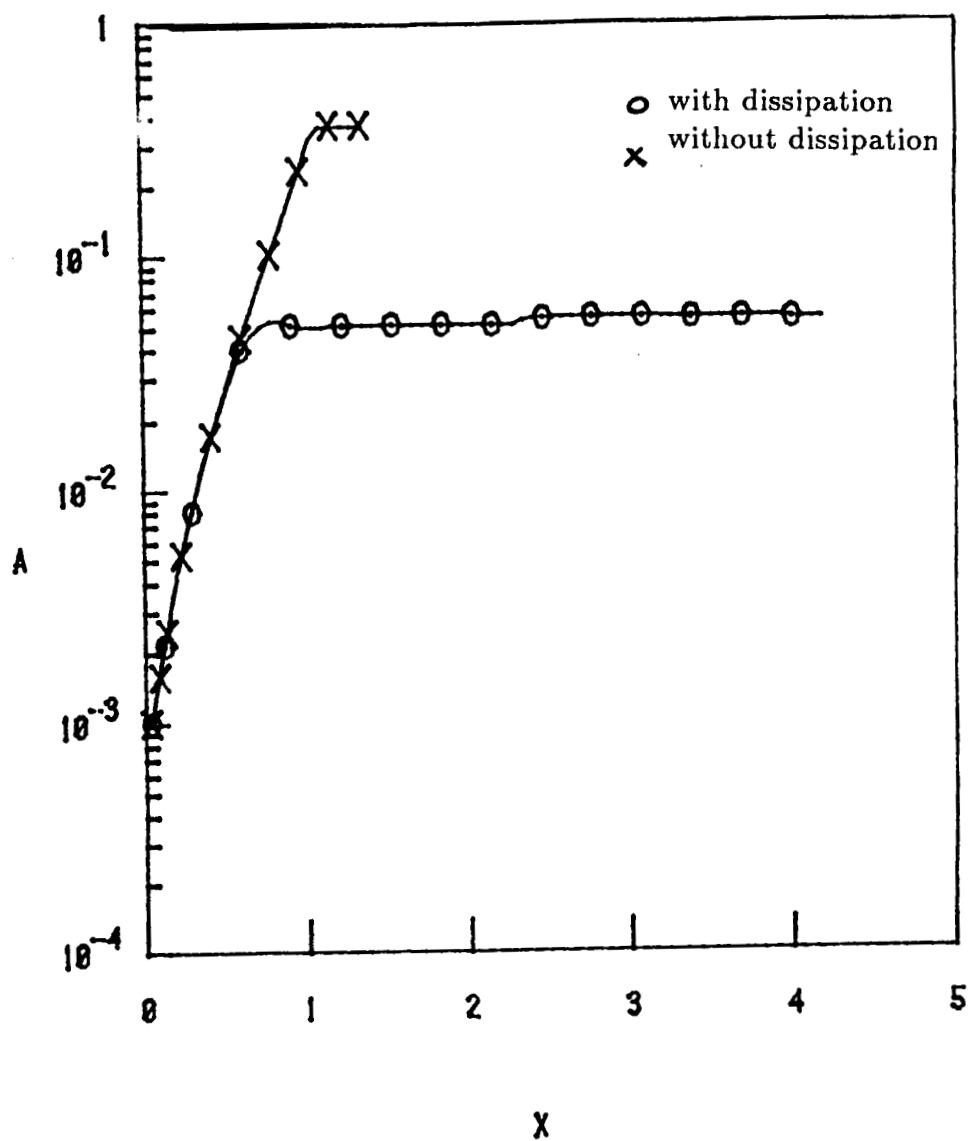


Figure 10: Variation of Wave Amplitude with Axial Distance.

the small-scale motions. The amplitude of the waves, therefore, grew essentially without limit. To verify this, we simulated the gross effects of this term by

$$- C \frac{k^{3/2}}{l}$$

where C is a constant and l is a local length scale. This is based on dimensional reasoning and the assumption that the γ_{ij} scale with the kinetic energy, k , of the wave motions. Part of the turbulent kinetic energy is then taken away from the motion of the wavy components and limits their amplitude. Figure 9 shows the development of the mean stream-wise velocity component calculated using this model. We also compared the variations of the wave amplitude in these two cases. The results are shown in figure 10. The amplitude function initially grows exponentially and then flattened. This agrees with experimental findings, ref. 8. Thus, a good model for these residual stresses is crucial since the coherent structures dominate the flow development and their amplitude must be determined. Unfortunately, little experimental data is available regarding these stresses.

Several approaches are now being developed to model this energy transfer mechanism. On-going efforts also include using the kinetic energy equation for the small-scale motion to estimate the velocity scale in the eddy viscosity model. The equation for the small-scale turbulent kinetic energy is

$$U_j \frac{\partial k'}{\partial x_j} = -\overline{u'_i u'_j} \frac{\partial u_i}{\partial x_j} - \frac{\partial}{\partial x_j} (\overline{u'_j k'}) + \frac{\overline{p' u'_j}}{\rho} + \overline{(- < -u'_i u'_j >)} \frac{\partial u_i}{\partial x_j} \\ - \overline{u_j \frac{\partial}{\partial x_j} < \frac{1}{2} u'_i u'_i >}} + \text{viscous terms}$$

Note that the equation must be solved simultaneously with the mean flow equations. Initially the modeling of each term in the equation is performed in a similar way to that of traditional closure schemes.

4. References

1. T. Theodorsen, "Theory of Wing Sections of Arbitrary Shape," *NACA Rep.* 411, 1931.
2. P. Henrici, *Applied and Computational Complex Analysis, Vol. 3*, John Wiley and Sons, 1986.
3. I. Garrick, "Potential Flow About Arbitrary Biplane Wing Sections," *NACA Rep.* 542, 1936.
4. M. Gutknecht, "Solving Theodorsen's Integral Equation for Conformal Maps with the Fast Fourier Transform and Various Nonlinear Iterative Methods," *Numer. Math.*, **36**, 1981.
5. P. J. Morris, T. R. S. Bhat, and G. Chen, "Shock Structure in Jets of Arbitrary Exit Geometry," *AIAA Paper No.*, 87-2697, 1987.
6. W.-W. Liou, "The Computation of Reynolds Stress in an Incompressible Plane Mixing Layer," *M. S. Thesis*, The Pennsylvania State University, 1986.
7. B. Latigo, "Large-scale Structure Interactions in a Two-dimensional Turbulent Mixing Layer," *Ph. D. Thesis*, University of South California, 1979.
8. R. W. Miksad, "Experiments on the Nonlinear Stages of Free-shear-layer Transition," *J. Fluid Mechanics*, **56**, 1972.